MoiréTac: A Dual-Mode Visuotactile Sensor for Multidimensional Perception Using Moiré Pattern Amplification

Kit-Wa Sou[1*], Junhao Gong[1*], Shoujie Li[1†],
Chuqiao Lyu[1], Ziwu Song[1], Shilong Mu[2], Wenbo Ding[1†]

***Abstract*— Visuotactile sensors typically employ sparse marker arrays that limit spatial resolution and lack clear analytical force-to-image relationships. To solve this problem, we present MoiréTac, a dual-mode sensor that generates dense interference patterns via overlapping micro-gratings within a transparent architecture. When two gratings overlap with misalignment, they create moiré patterns that amplify microscopic deformations. The design preserves optical clarity for vision tasks while producing continuous moiré fields for tactile sensing, enabling simultaneous 6-axis force/torque measurement, contact localization, and visual perception. We combine physics-based features (brightness, phase gradient, orientation, and period) from moiré patterns with deep spatial features. These are mapped to 6-axis force/torque measurements, enabling interpretable regression through end-to-end learning. Experimental results demonstrate three capabilities: force/torque measurement with R^2>0.98 across tested axes; sensitivity tuning through geometric parameters (threefold gain adjustment); and vision functionality for object classification despite moiré overlay. Finally, we integrate the sensor into a robotic arm for cap removal with coordinated force and torque control, validating its potential for dexterous manipulation.**

I. INTRODUCTION

Robotic manipulation benefits from visuotactile sensing, where cameras observe elastic deformations to reveal texture, contact location, and force cues (e.g., GelSight [1], DIGIT [2], GelSlim [3]). Many existing systems still rely on sparse marker patterns and largely data-driven inference. Sparse sampling can limit information density and differentiability, which may hamper 6-axis force/torque estimation and complicate calibration and cross-talk analysis in dynamic tasks such as pressing, shearing, and unscrewing [4], [5]. In practice, robots also need vision cues before and during contact to localize targets and keep task context [6], while tactile cues should quantify forces once contact is made. Bridging these two regimes with a unified sensor and a physics-informed mapping remains challenging.

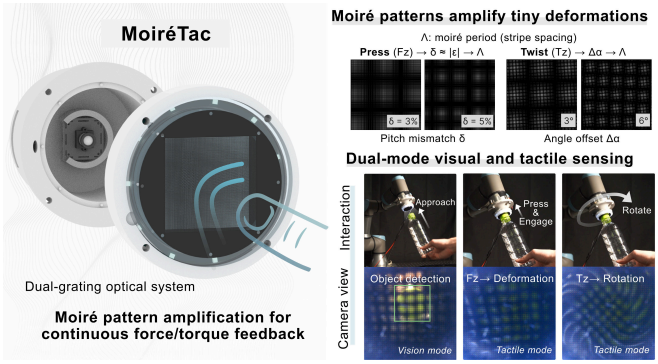

Fig. 1. Overview of MoiréTac. The dual-grating optical system generates moiré observables, which are mapped to force/torque measurements. The top-left panels show how press and rotation affect stripe density and orientation. The application demonstrates dual-mode visual and tactile sensing during robotic manipulation.

Moiré patterns, formed by the interference of two slightly misaligned periodic structures, provide dense fields that are sensitive to microscopic deformation [7]. Relative to sparse marker readout [8], this representation supplies pixel-level observables that support direct feature extraction for force/torque estimation [9], [10]. In our experiments, this dense design yields three measurable benefits: tunable sensitivity across grating configurations (about threefold gain change), high multi-axis regression quality ($R^2 > 0.98$ across six axes), and stable operation in dual-mode manipulation with forces beyond the low-force characterization range [11].

In this paper, we introduce **MoiréTac**, a compact visuotactile sensor that converts small deformations into a dense moiré field using a double-grid optic (Fig. 1). Our study presents three major contributions:

- **Moiré interferometry for visuotactile sensing:** We apply moiré pattern amplification to transform marker-based sensing into continuous interference fields, achieving $R^2 > 0.98$ across six force/torque axes. Unlike sparse marker methods that interpolate between discrete points, our continuous fields directly encode mechanical deformations at every pixel.
- **Physics-informed force/torque framework:** We establish analytical mappings from four moiré observables (I, $\nabla\phi$, θ, Λ) to 6-axis wrench, enabling sensitivity adjustment through geometric parameters. This interpretable approach permits analytical sensitivity analysis and systematic calibration transfer, which are difficult

*These authors contributed equally to this work.

This work was supported by National Key R&D Program of China (No.2024YFB3816000), Shenzhen Key Laboratory of Ubiquitous Data Enabling (No. ZDSYS20220527171406015), Guangdong Innovative and Entrepreneurial Research Team Program (2021ZT09L197), and Tsinghua Shenzhen International Graduate School-Shenzhen Pengrui Young Faculty Program of Shenzhen Pengrui Foundation (No. SZPR2023005).

†Corresponding author: Shoujie Li (lsj20@mails.tsinghua.edu.cn), Wenbo Ding (ding.wenbo@sz.tsinghua.edu.cn)

[1]Shenzhen Ubiquitous Data Enabling Key Lab, Shenzhen International Graduate School, Tsinghua University, Shenzhen 518055, China.

[2]Xspark Ai, Shenzhen, China.

This paper has supplementary downloadable material available at: https://MoireTac.github.io/

to obtain with purely black-box models.

- **Transparent dual-mode operation:** We maintain optical transparency for object recognition while measuring forces, demonstrated in automated cap removal tasks. The preserved visual channel operates concurrently with tactile sensing, unlike opaque sensors that lose visual information upon contact.

II. RELATED WORK

In visuotactile sensing, an onboard camera images an elastic medium under contact, converting deformations into spatial measurements (e.g., GelSight [1], DIGIT [2], GelSlim [3]) [12], [13]. Comprehensive reviews [4], [5], [12]–[15] report common limitations in many systems: sparse marker arrays that undersample contact regions, and force mappings with limited physical interpretability. These factors complicate 6-axis force/torque estimation and cross-device calibration transfer.

Recent systems [16]–[21] employ deep networks to directly regress forces from tactile images, achieving strong accuracy in controlled settings. Yet these data-driven approaches can struggle with generalization across devices and may require extensive calibration [22], [23]. Limited use of physics-informed representations can also hinder multi-axis decoupling, because purely learned mappings do not explicitly exploit analytical image-to-mechanics relationships.

Moiré interferometry offers an alternative via optical amplification of microscopic deformations [7]. Unlike discrete markers, moiré fringes produce continuous fields whose period, orientation, and phase relate analytically to mechanical quantities [24], enabling sub-micron precision in structural monitoring and nano-positioning. For tactile use, traditional moiré force visualizers remain qualitative and parallax-prone; fiber–optic plates mitigate parallax yet still prioritize visual readout over dense 6-DoF estimation [26]. Meanwhile, MoiréVision [25] demonstrated 6-DoF tracking with moiré cues, suggesting that calibrated moiré parameters can yield dense, interpretable measurements for advanced tactile sensing, including force/torque inference [9], [10].

Multimodal designs combining vision and touch typically require separate optical paths or complex multiplexing [27]–[32], increasing system complexity. Transparent sensors could preserve visual channels through the tactile medium, yet existing approaches sacrifice either optical clarity or tactile resolution [27], [29].

MoiréTac addresses these gaps by: (1) replacing sparse markers with continuous moiré fields for dense spatial measurements, (2) establishing analytical mappings from four moiré observables to 6-axis forces/torques, and (3) maintaining optical transparency for dual-mode vision-tactile operation. This physics-informed approach bridges precision measurement with learning-based adaptability.

III. DESIGN AND IMPLEMENTATION

MoiréTac addresses sparse sampling and limited physical interpretability in current visuotactile sensors through moiré interferometry. The continuous interference patterns provide dense, differentiable signals with optical theory linking image features to mechanical loads.

A. Design Principle

MoiréTac exploits moiré interferometry to transform microscopic deformations into continuous visual signatures. Two stacked micro-gratings create an optical system where mechanical changes modulate fringe patterns that encode the complete 6-axis wrench through four observables: intensity I, phase gradient $\nabla\phi$, fringe orientation θ, and period Λ.

Mathematical Foundation: Each grating functions as a spatial harmonic filter, and modulates the intensity distribution in space. The grating intensity distribution is described by:

$$g_i(\mathbf{x}) = \cos(\mathbf{k}_i \cdot \mathbf{x}), \quad \mathbf{k}_i = \tfrac{2\pi}{p_i}[\cos\alpha_i, \sin\alpha_i]^\top, \tag{1}$$

where p_i and α_i define pitch and orientation. When overlapped, they generate a beat pattern with moiré wavevector

$$\mathbf{K} = \mathbf{k}_1 - \mathbf{k}_2, \quad \Lambda = \frac{2\pi}{\|\mathbf{K}\|}, \quad \theta = \operatorname{atan2}(K_y, K_x). \tag{2}$$

This immediately provides us with the period Λ and orientation θ as directly measurable observables.

Normal Force via Optical Coupling (Fig. 2a): When a hemispherical indenter (mimicking fingertip contact) is pressed onto the surface, Poisson contraction induces lateral strain ε, which modulates the pitch mismatch and thus the moiré period, encoding the normal force.

$$I(\mathbf{x}) \approx I_0 + \kappa\,(P * h)(\mathbf{x}), \quad \Lambda' \approx \frac{p}{\delta'}, \;\; \delta' \approx |\varepsilon(F_z)|, \tag{3}$$

where $P * h$ represents the pressure field convolved with the optical point spread function. This dual response makes F_z particularly robust; note that the net fringe trend under compression is set by Eq. (7).

Shear Forces via Phase Tracking (Fig. 2b): Moiré fringes are highly sensitive to lateral motion. Any local displacement $\mathbf{u}(\mathbf{x})$ directly modulates the fringe phase:

$$\phi(\mathbf{x}) \approx \mathbf{K}\cdot\mathbf{x} + \mathbf{K}\cdot\mathbf{u}(\mathbf{x}). \tag{4}$$

The spatial averages of phase gradients $\langle\partial_x\phi\rangle$ and $\langle\partial_y\phi\rangle$ encode the net shear forces F_x and F_y, providing precise displacement sensitivity. While physical contact requires normal preload to generate shear, our simulation isolates the lateral response to demonstrate phase modulation under pure shear loading.

Geometric Design Space (Fig. 2c): The sensor's sensitivity is tunable through geometric parameters. The general period relationship:

$$\Lambda = \frac{p_1 p_2}{\sqrt{p_1^2 + p_2^2 - 2p_1 p_2 \cos\Delta\alpha}} \tag{5}$$

simplifies to two practical design regimes:

$$\Lambda \approx \frac{p}{\Delta\alpha} \quad \text{(angle-dominated)}, \quad \Lambda = \frac{p}{\delta} \quad \text{(pitch-dominated)}, \tag{6}$$

where $p = (p_1{+}p_2)/2$ and $\delta = |p_2{-}p_1|/p$. Smaller $\Delta\alpha$ or δ yields larger Λ (greater geometric magnification A).

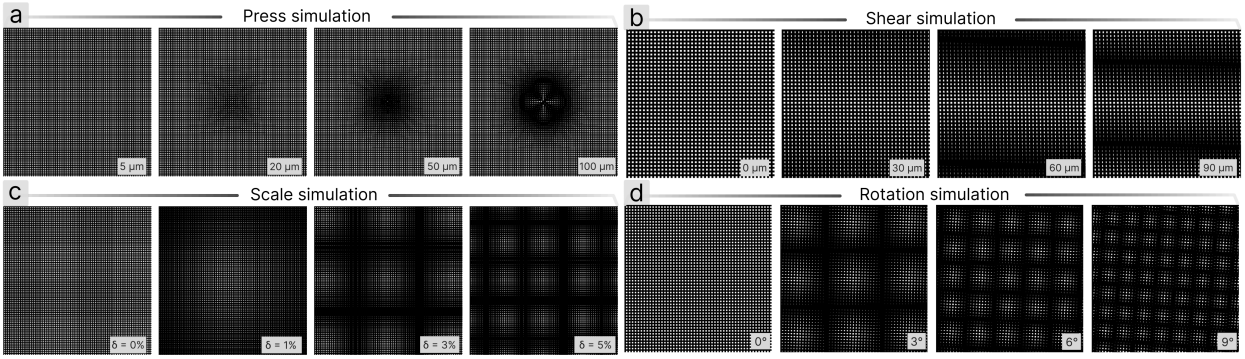

Fig. 2. Simulation panels: (a) Press simulation with displacements of 5 μm to 100 μm. (b) Shear simulation with displacements from 0 μm to 90 μm. (c) Scale simulation with scaling variations from 0% to 5%. (d) Rotation simulation with angular shifts from 0° to 9°. All displacements and rotations represent the changes in the moiré patterns, used to simulate different types of mechanical deformations.

$$\delta_{\text{eff}} \approx \left|\delta_{\text{obj}} - a/Z\right|, \tag{7}$$

with inter-grating spacing a and camera distance Z. Under compression, the sign of $\delta_{\text{obj}} - a/Z$ sets the trend: if $\delta_{\text{obj}} < a/Z$, then δ_{eff} decreases and Λ increases (sparser); if $\delta_{\text{obj}} > a/Z$, the opposite holds (denser).

Moment Sensing via Pattern Morphology (Fig. 2d): Torques manifest through distinct fringe transformations. Twist T_z simply rotates the entire pattern:

$$\Delta\theta \approx \Delta\alpha \;\propto\; T_z. \tag{8}$$

Tilting moments T_x, T_y create asymmetric pressure distributions, shifting the brightness centroid $\mathbf{c} = \langle \mathbf{x} \rangle_I$:

$$[T_x, T_y]^\top \approx \mathbf{M}\,(\mathbf{c} - \mathbf{c}_0), \tag{9}$$

where $\mathbf{M}$ is a calibrated mapping matrix. Table I summarizes these physics-guided relationships, forming our compact feature pipeline. These analytical relationships guide the sensor's physical implementation, where geometric parameters and material properties must be carefully orchestrated.

TABLE I
MAPPING OF MOIRÉ OBSERVABLES TO FORCE/TORQUE MEASUREMENTS

Axis	Primary observable & physical mechanism
F_z	Brightness I rises with contact; period Λ varies via strain coupling Eq. (3)
F_x, F_y	Phase gradients $\langle \nabla\phi \rangle$ track lateral displacement fields Eq. (4)
T_z	Orientation θ rotates directly with applied twist Eq. (8)
T_x, T_y	Brightness centroid $\mathbf{c}$ shifts under asymmetric loading Eq. (9)

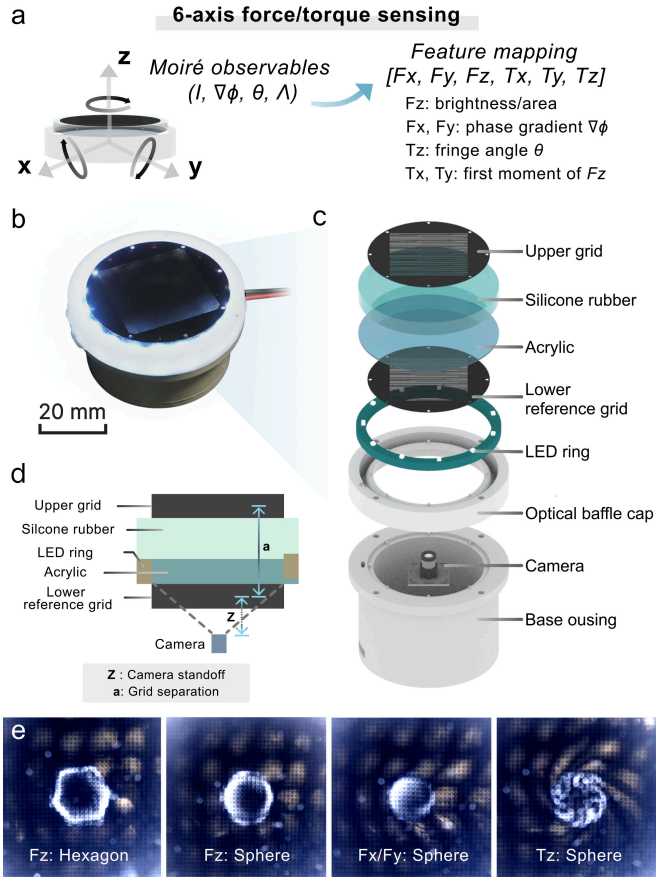

Fig. 3. Structure illustration. (a) Mapping from Moiré observables (intensity I, phase $\nabla\phi$, angle θ, period Λ) to 6-axis force/torque sensing. (b) Photo of prototype. (c) Exploded view of layered architecture. (d) Cross-section showing compression–to–fringe coupling. (e) Responses under normal, shear, and twist loading; a waveguided LED produces a contact rim that delineates the boundary and maintains fringe visibility.

B. Mechanical Stack and Structure

To realize these optical principles (Fig. 3a), MoiréTac employs a compact layered architecture that transforms microscopic deformations into high-contrast moiré patterns (Fig. 3b). The sensor achieves 4–24× mechanical-to-optical amplification by exploiting interference between two micro-gratings separated by a compliant medium. The layered architecture (Fig. 3c) integrates optical and mechanical functions: a deformable upper grating moves with applied loads, while a fixed lower reference grating provides the interferometric baseline; a silicone elastomer bonded to an acrylic carrier offers compliance and transparency; an LED ring with a shallow baffle ensures uniform illumination; and a bottom camera captures the resulting fringes.

The key mechanism lies in the inter-grating spacing a

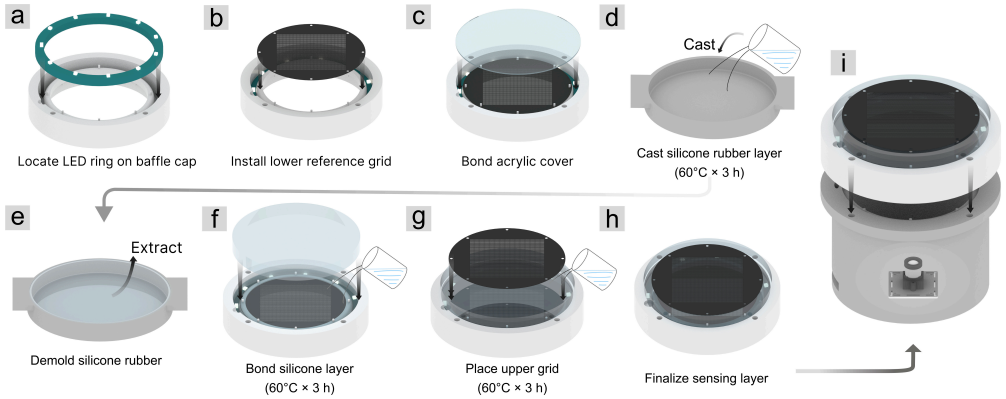

Fig. 4. Fabrication process of MoiréTac sensor showing assembly steps. (a-c) Optical base assembly with LED ring positioning on baffle cap, lower reference grid installation, and acrylic cover bonding. (d-f) Elastomer layer preparation including silicone casting at 60°C for 3 hours, demolding, and thermal bonding to acrylic substrate. (g-h) Sensing layer completion with upper grid placement and final assembly. (i) Fully integrated sensor with camera.

(Fig. 3d). Under compression, a decreases and induces Poisson-driven lateral strain, which modulates the pitch mismatch δ and hence the moiré period Λ, encoding the normal force. Lateral shifts produce fringe translations that encode shear forces. An LED ring waveguided through silicone rubber forms a bright contact rim whose integrated brightness/area rises with compression, thereby localizing contact (Fig. 3e). This photometric rim provides a visual boundary cue that is distinct from the tactile moiré features. The same illumination mitigates fringe visibility loss in the dark annulus under stronger compression. Finally, we preset a small δ to ensure robust phase extraction (Sec. III-D).

C. Fabrication

MoiréTac assembly follows an eight-step procedure (Fig. 4); Table II lists components for the grating set used in subsequent experiments. The optical base assembly (a–c) begins with positioning the LED ring on the baffle cap, installing the lower reference grid at the focal plane, and bonding an acrylic cover using cyanoacrylate adhesive to create a flat carrier platform.

The sensing layer (d–h) uses PDMS elastomer (30:1 ratio) cast onto the acrylic substrate and cured at 60 °C for 3 hours. After demolding, the elastomer is thermally bonded to the acrylic. The upper grid is positioned with a controlled pitch difference δ relative to the lower grid, which generates magnified moiré patterns. Critical parameters include grid alignment ($\pm 0.5°$) and uniform elastomer thickness.

D. Sensitivity Tuning through Geometric Design

MoiréTac's phase sensitivity is governed by the effective pitch mismatch δ_{eff} (Eq. 7), which combines the intrinsic mismatch δ_{obj} with the fixed depth separation, so larger δ_{eff} shortens the moiré period Λ and increases fringe density, thereby enhancing sensitivity. All three configurations satisfy $\delta_{\text{obj}} < a/Z$, so compression increases Λ (sparser). We evaluate three pitch pairs (near grid at Z with pitch p_2; far grid at $Z + a$ with pitch p_1; $a/Z = 0.25$), matching the panel tags in Fig. 5a: Dense $(p_1, p_2) = (0.20, 0.20)\,\text{mm}$ gives $A = 4.00$ and $\delta_{\text{eff}} = 0.25$; Mid $(0.35, 0.30)$ gives $A = 14.00$ and $\delta_{\text{eff}} = 0.10$; Sparse $(0.30, 0.25)$ gives $A = 24.00$ and $\delta_{\text{eff}} = 0.07$. As fringe density decreases from Dense to Sparse (Fig. 5b), sensitivity decreases accordingly; note that A increases, but the readout is governed by fringe density. Selecting δ at fabrication thus tunes the sensitivity–range trade-off: denser fringes increase sensitivity but narrow range; sparser widen range but reduce sensitivity. We adopt Mid for balance.

TABLE II
BILL OF MATERIALS FOR MOIRÉTAC SENSOR

Component	Description	Process
Optical Components		
Camera	IMX258, 12MP, 120° FOV	Off-the-shelf
Upper grid	350 µm pitch on black NBR	Laser ablation
Lower reference grid	300 µm pitch on black NBR	Laser ablation
LED ring	40 mm dia., white LEDs	Off-the-shelf
Structural Components		
Base housing	PLA, 45 mm dia.	3D printing
Optical baffle cap	PLA, 45 mm dia.	3D printing
Camera mount	PLA, M12 thread	3D printing
Elastomer Assembly		
Acrylic	1 mm clear sheet	Laser cutting
Silicone rubber	PDMS 30:1, 3 mm thick	Molding
Adhesive	Cyanoacrylate 502	Manual
Raw Materials		
Nitrile rubber sheet	Black NBR, 0.5 mm thick	Die cutting

Compared with sparse-marker pipelines, the dense moiré field provides observables over the full contact area rather than at discrete keypoints. This design directly supports the three requirements emphasized in this paper: tunable gain (Fig. 5), low axis coupling under isolated calibration (Fig. 7), and stable operation in higher-load manipulation tasks (Sec. IV-D).

E. Sensing Pipeline

Image Preprocessing. Although the 120° lens introduces minimal distortion, we perform a one-time calibration to establish the pixel-to-millimeter mapping and define the 30×30 mm sensing region (Fig. 6). A cylinder array pressed

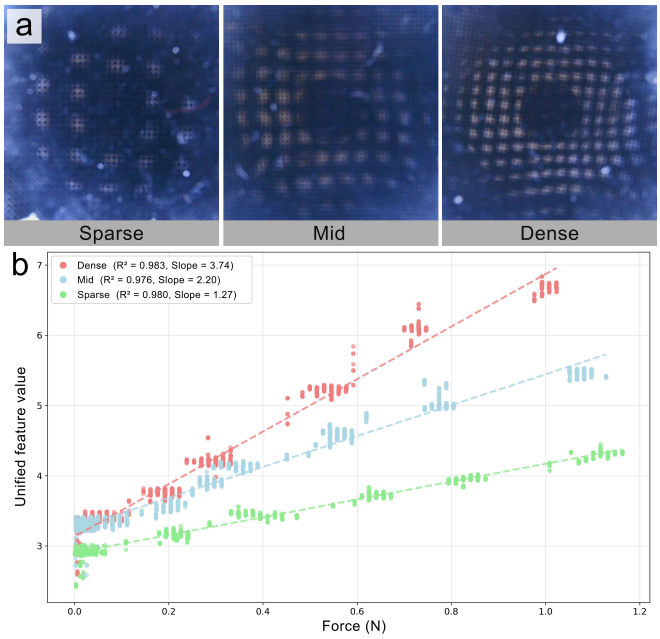

Fig. 5. Sensitivity modulation via pitch difference δ. (a) Moiré patterns under three design configurations showing increasing fringe density, with the central dark circle indicating the robot arm's shadow. (b) Force–response curves demonstrating tunable sensitivity.

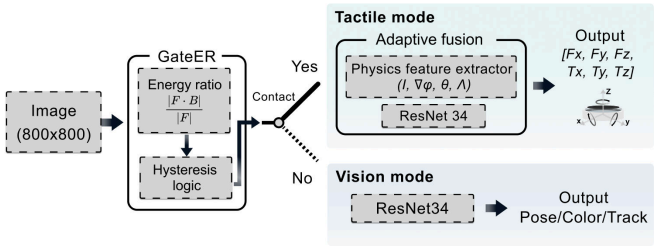

Fig. 6. Overview of the MoiréTac processing pipeline.

onto the sensor creates reference points for cropping and scaling the raw image to a standardized 800×800 pixel format (20 pixels/mm), ensuring consistent input dimensions for the neural network and preserving spatial alignment.

Dual-Mode Processing. The system employs a GateER (Gated Energy Ratio) module, which computes an energy metric from the moiré pattern to detect contact. The module uses an adaptive threshold mechanism with approximately 20% hysteresis margin to prevent mode oscillation, achieving typical switching response times of 30-40 ms. The hysteresis logic settings need to be tuned based on specific application requirements. In vision mode (no contact), ResNet34 processes the undistorted moiré pattern as a textured background for pose estimation, color recognition, and object tracking. Upon contact detection, the system switches to tactile mode, activating an adaptive fusion mechanism that interprets fringe deformations as mechanical signals for real-time force sensing at camera frame rate.

Force/Torque Regression. Upon switching to tactile mode, MoiréTac employs an adaptive fusion architecture that processes calibrated images through dual parallel pathways. The physics feature extractor computes four primary observables, brightness I, phase gradients $\nabla\phi$, orientation θ, and period Λ, based on moiré theory relationships (Table I), while ResNet34 independently extracts deep spatial features. These complementary representations merge before the final regression layers, combining physics-based constraints with data-driven pattern recognition. This hybrid approach leverages the interpretability of moiré theory while allowing the network to learn complex nonlinearities and cross-axis couplings beyond simplified analytical models. The network outputs a 6-dimensional vector $[F_x, F_y, F_z, T_x, T_y, T_z]$ through modified fully connected layers. ResNet34's residual connections work well for moiré patterns, preserving both fine-grained local variations and global fringe structures in the architecture.

IV. Experimental Evaluation

A. Force/Torque Characterization

We validate MoiréTac against a commercial F/T sensor (Fig. 7a) under laboratory white light conditions. A 6-DoF robot applies controlled loads while both sensors are recorded synchronously at 60 Hz; frames and F/T readings are time-aligned and downsampled to the camera rate. We collected approximately 10,000 image-force pairs over multiple sessions, with uniform sampling across each axis's operating range. Each axis is calibrated in isolation to reduce coupling: (i) normal indentations for F_z (0–1.2 N); (ii) lateral sliding for F_x, F_y ($\pm$0.2 N) under a constant preload; (iii) axial rotation about the sensor center for T_z ($\pm$0.008 Nm); and (iv) off-center indentations at multiple locations for T_x, T_y ($\pm$0.012 Nm). Rectified 800×800 grayscale images are fed to a physics-informed ResNet-34 for regression. The dataset was split 80/20 for training and testing, with stratification across load levels and contact locations.

To support the manipulation loads in Sec. IV-D, we additionally collected an extended-range dataset using the same setup and reference sensor, including normal forces up to 10 N. The controller in Sec. IV-D uses this extended-range calibration, while Fig. 7 reports the low-force subset to highlight linearity and decoupling.

Results demonstrate agreement across all six axes (Fig. 7b,c). Forces achieve $R^2 \geq 0.99$ (F_z: $R^2 = 0.992$, MAE $= 0.25$ N). Torque estimation shows strong T_z accuracy due to direct fringe-rotation coupling ($R^2 = 0.999$, MAE $= 1 \times 10^{-3}$ Nm), while tilt moments T_x, T_y maintain $R^2 > 0.98$. The tight clustering along identity lines indicates low cross-talk between axes under isolated loading conditions on the prototype.

B. Visual Sensing

Unlike opaque tactile sensors that occlude the contact area, MoiréTac's transparent dual-grating architecture preserves the visual channel. Although moiré fringes overlay the scene, they behave as high-frequency spatial modulation that can be attenuated with standard frequency-domain notch filtering or handled directly by learning-based recognition models. This transparency enables pre-contact identification

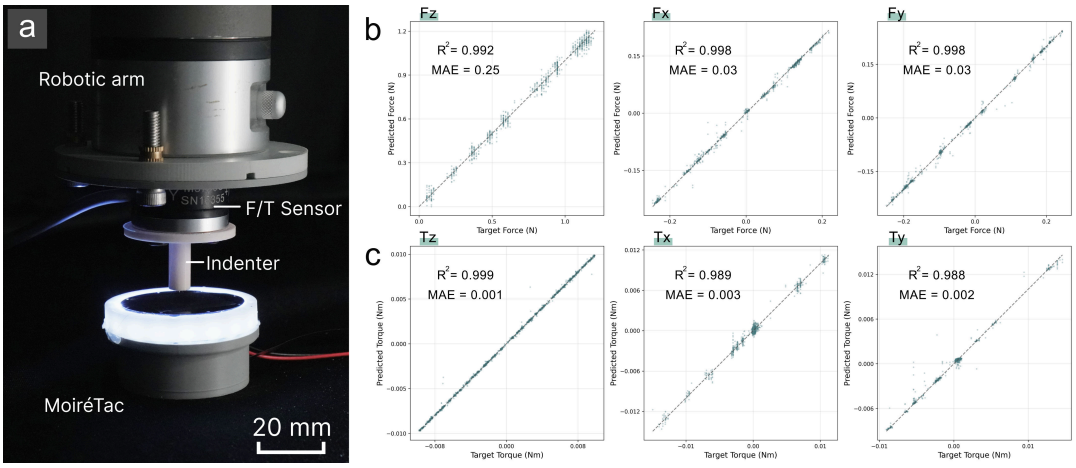

Fig. 7. Six-axis force/torque calibration. (a) Experimental setup with robotic arm, commercial F/T reference, and MoiréTac prototype. (b) Force calibration showing linearity for normal force F_z and shear forces F_x, F_y. (c) Torque calibration demonstrating T_z and T_x, T_y performance.

and alignment, which are critical when grasping unfamiliar objects or targeting specific surface features.

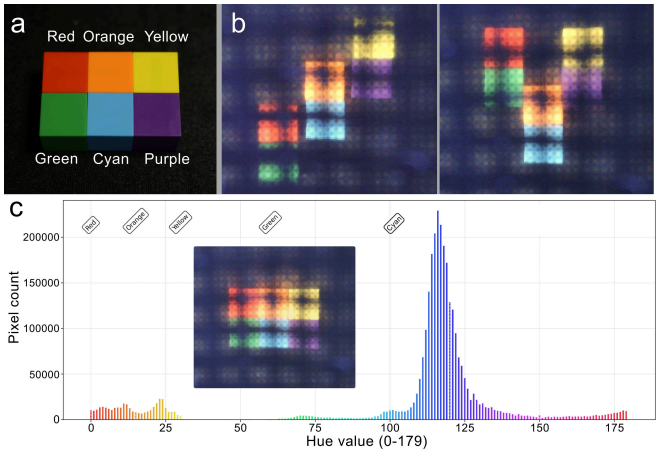

Fig. 8. Color perception in vision mode. (a) Reference cube with six colors. (b) Images captured under two poses; the colored surface is visible on top of the moiré background. (c) Hue histogram in HSV (OpenCV scale 0–179) aggregated over the patches; distinct peaks for red, orange, yellow, green, cyan, and purple indicate separability for identification.

We validate color fidelity using a standard six-color card (Fig. 8a). Despite transmission through two micro-gratings and an elastomer layer, colors remain clearly distinguishable (Fig. 8b). The HSV hue histogram (Fig. 8c) shows well-separated peaks with limited overlap between adjacent classes. The moiré pattern introduces periodic intensity modulation yet preserves underlying spectral content, enabling effective color-based segmentation.

Object recognition tests with six fruits/vegetables demonstrate practicality (Fig. 9a). We collected 900 samples for each of six fruits in 3 different orientations at 60 Hz, capturing 5 seconds per orientation. The dataset was divided using an 80/20 train-test split. Distinct color–texture cues remain visible through the sensor (Fig. 9b): e.g., lime's uniform green, bitter melon's ridges, banana's smooth yellow curve, peach's gradient, kiwi's brown fuzz, and corn's kernel regularity. A ResNet34 classifier achieves high accuracy (Fig. 9c), reaching 100% accuracy on our test set without requiring specialized preprocessing to remove moiré artifacts.

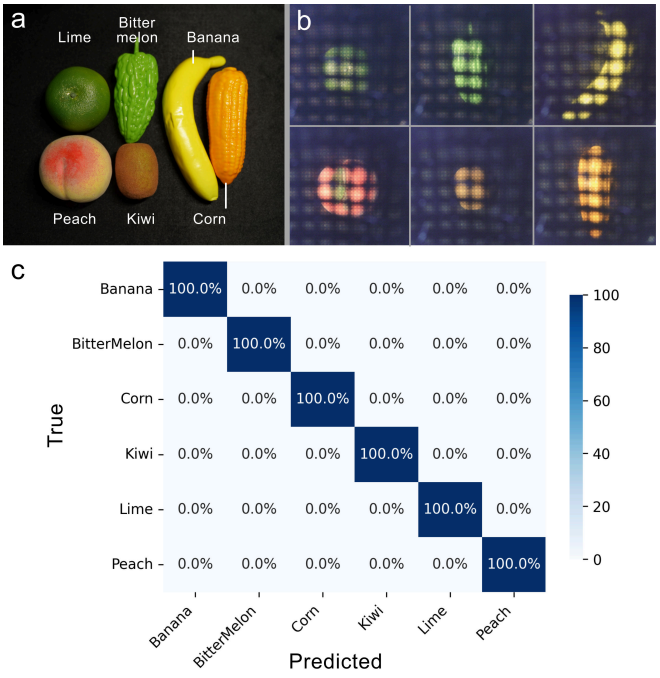

Fig. 9. Vision-mode object recognition. (a) Six target fruits. (b) Representative sensor images where color appearance is visible over the moiré background. (c) Confusion matrix of trained classifier on test set

C. Dual-Mode Manipulation Tasks

To demonstrate MoiréTac's vision-tactile integration, we evaluate the sensor on a bottle cap removal task requiring both modalities and real-time feedback (Fig. 10a). This manipulation sequence showcases automatic mode switching based on contact state and highlights the value of preserving visual feedback throughout the task.

The task proceeds through four phases with automatic mode transitions (Fig. 10b). Initially in vision mode, the

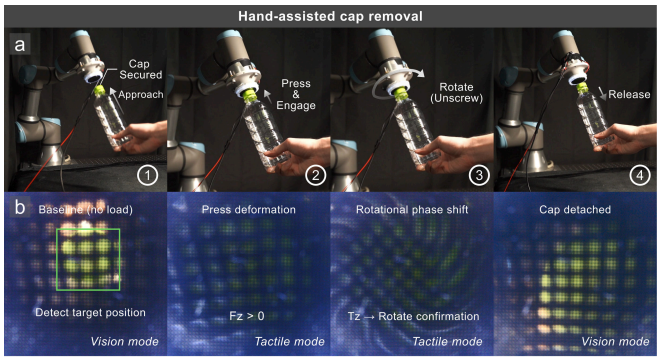

Fig. 10. Hand-assisted cap removal demonstrating dual-mode operation. (a) Task sequence: (1) vision-guided approach to locate cap, (2) press to establish grip with force feedback, (3) rotate to unscrew with torque monitoring, (4) release after completed removal. (b) Corresponding sensor views showing vision-tactile mode transitions. Green box indicates visual target detection, while moiré patterns reveal force/torque during manipulation.

sensor identifies the green cap position through color segmentation despite moiré overlay. Upon approach and contact (phase 2), the system switches to tactile mode, where fringe deformation confirms sufficient normal force ($F_z > 0$) for secure grip. During rotation (phase 3), the sensor tracks twist torque T_z through fringe orientation changes, providing feedback for controlled unscrewing. After cap removal (phase 4), the sensor returns to vision mode, confirming task completion through visual verification.

This hand-assisted demonstration validates four capabilities: vision mode for object tracking, tactile mode for force/torque feedback during manipulation, automatic mode switching to eliminate blind spots common in opaque sensors, and the use of the same optical path for both sensing modalities without requiring mechanical reconfiguration. The continuous visual feedback enables error detection and recovery, as the operator can observe both the target and contact state simultaneously.

D. Automated Force-Controlled Manipulation

We extend the dual-mode capability to automated robotic manipulation, demonstrating a precise force-controlled cap removal with fixed-base bottles. This experiment quantifies MoiréTac's ability to maintain consistent force/torque profiles through an incremental rotation strategy that prevents slippage and cumulative errors.

The robotic system employs an incremental rotation strategy, repeating a four-phase control cycle until complete cap removal (Fig. 11a,b). This incremental approach prevents slip accumulation that continuous rotation would cause, with each cycle executing a partial rotation under controlled force limits to ensure consistent grip throughout the unscrewing process. For the timeline shown in Fig. 11c, Phase 1 uses vision mode to align within the cap perimeter. Upon contact detection ($F_z > 0.5\,\mathrm{N}$), phase 2 gradually increases normal force to $6\,\mathrm{N}$ for secure grip, using the extended-range calibration described in Sec. IV-A. During rotation (phase 3), the system executes a controlled partial turn while monitoring T_z for thread resistance and continuously adjusting height

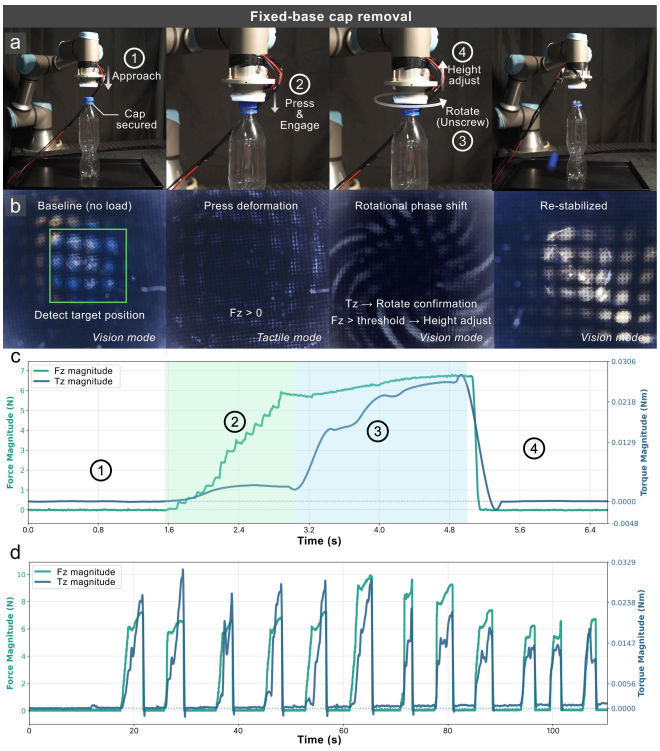

Fig. 11. Fixed-base automated cap removal. (a) Robotic execution sequence for each rotation cycle: (1) vision-guided approach, (2) press and engage, (3) controlled partial rotation with height adjustment, (4) release. (b) Sensor views showing vision-to-tactile transitions with force/torque feedback. (c) Single rotation cycle timeline showing coordinated F_z and T_z control during phases 1–4 (6.4 s). (d) Complete cap removal timeline showing 12 incremental rotation over 112 s.

to accommodate the cap's upward displacement as threads disengage. Phase 4 releases the cap, allowing vision mode to verify rotation progress before the next cycle.

The complete removal process (Fig. 11d) requires approximately 12 rotation cycles over 112 s, successfully demonstrated in repeated trials (N=30). Each peak corresponds to one grip–rotate–release sequence, with consistent force profiles: mean peak $F_z = 7.2 \pm 0.8\,\mathrm{N}$ and mean peak $T_z = 0.024 \pm 0.003\,\mathrm{Nm}$ per cycle. Early cycles show higher torque resistance as threads are fully engaged, while later cycles exhibit reduced resistance as the cap loosens. Cycle 5 exhibits the highest peaks ($10\,\mathrm{N}$, $0.032\,\mathrm{Nm}$), likely due to thread binding, yet the system maintains control through force-limited operation.

This incremental approach offers advantages including: (i) preventing accumulated slip errors through periodic re-gripping, (ii) enabling visual verification between cycles, (iii) maintaining target grip force without sensor drift, and (iv) adapting to varying thread resistance throughout removal. The consistent force/torque ratio ($T_z/F_z \approx 0.003\,\mathrm{m}$) across cycles is consistent with the low cross-talk trend observed in isolated calibration. Vision mode re-engagement between cycles (visible as brief returns toward baseline) provides continuous task monitoring. This automated demonstration confirms MoiréTac provides the sensitivity, dynamic range, and dual-mode capability suitable for dexterous manipulation

requiring coordinated force-torque control.

V. Conclusions

In this paper, we present MoiréTac, a transparent visuotactile sensor that uses moiré amplification for dense, physics-informed 6-axis force/torque sensing. We link four moiré observables (intensity, phase gradient, orientation, and period) to wrench components and fuse them with deep features for regression. Experiments show $R^2 > 0.98$ on all axes and $R^2 > 0.99$ for twist, nearly threefold sensitivity tuning via geometric design, and robust color/object perception despite moiré overlays. In manipulation, both hand-assisted and automated cap-removal are completed with stable force control (mean peak $F_z = 7.2 \pm 0.8\,\mathrm{N}$) using incremental rotation.

The current 45 mm rigid design targets parallel-jaw grippers, while alternative form factors can support curved or miniaturized end-effectors. The bill of materials is dominated by off-the-shelf optics and simple laser-cut/3D-printed parts, enabling low-cost prototyping and small-batch scaling. For scenarios prioritizing visual clarity, moiré texture can be attenuated by software filtering. Future work includes nanoimprinted gratings for flexible sensors, elastomer variants for wider temperature ranges, stronger cross-device robustness, and physics-informed learning for better data efficiency. Overall, MoiréTac offers a practical dual-mode sensing route for quality inspection, collaborative manipulation, and precision assembly.

References

[1] W. Yuan, S. Dong, and E. H. Adelson, "GelSight: High-resolution robot tactile sensors for estimating geometry and force," *Sensors*, vol. 17, no. 12, 2017.

[2] M. Lambeta et al., "DIGIT: A novel design for a low-cost compact high-resolution tactile sensor with application to in-hand manipulation," *IEEE Robotics and Automation Letters*, vol. 5, no. 3, pp. 3838–3845, 2020.

[3] D. Ma, E. Donlon, S. Dong, and A. Rodriguez, "Dense tactile force estimation using GelSlim and inverse FEM," in *2019 International Conference on Robotics and Automation (ICRA)*, 2019, pp. 5418–5424.

[4] Z. Kappassov, J.-A. Corrales, and V. Perdereau, "Tactile sensing in dexterous robot hands," *Robotics and Autonomous Systems*, vol. 74, pp. 195–220, 2015.

[5] K. Shimonomura, "Tactile image sensors employing camera: A review," *Sensors*, vol. 19, no. 18, p. 3933, 2019.

[6] R. Li, R. Platt, W. Yuan, A. ten Pas, N. Roscup, M. A. Srinivasan, and E. Adelson, "Localization and manipulation of small parts using GelSight tactile sensing," in *2014 IEEE/RSJ International Conference on Intelligent Robots and Systems (IROS)*, 2014, pp. 3988–3993.

[7] S. S. Dindorkar, A. S. Kurade, and A. H. Shaikh, "Magical moiré patterns in twisted bilayer graphene: A review on recent advances in graphene twistronics," *Chemical Physics Impact*, vol. 7, p. 100325, 2023.

[8] V. Saveljev, J. Kim, J.-Y. Son, Y. Kim, and G. Heo, "Static moiré patterns in moving grids," *Scientific Reports*, vol. 10, no. 1, p. 14414, 2020.

[9] P.-H. Tsai and Y.-Y. Chuang, "Target-driven moire pattern synthesis by phase modulation," in *Proceedings of the IEEE International Conference on Computer Vision*, 2013, pp. 1912–1919.

[10] K. Creath and J. C. Wyant, "Moiré and fringe projection techniques," *Optical Shop Testing*, vol. 2, pp. 653–685, 1992.

[11] I. Choi, S. J. Yoon, and Y.-L. Park, "Linear electrostatic actuators with Moiré-effect optical proprioceptive sensing and electroadhesive braking," *The International Journal of Robotics Research*, vol. 43, no. 5, pp. 646–664, 2024.

[12] S. Li et al., "When vision meets touch: A contemporary review for visuotactile sensors from the signal processing perspective," *IEEE Journal of Selected Topics in Signal Processing*, vol. 18, no. 3, pp. 267–287, 2024.

[13] H. Li, Y. Lin, C. Lu, M. Yang, E. Psomopoulou, and N. F. Lepora, "Classification of vision-based tactile sensors: A review," *IEEE Sensors Journal*, 2025.

[14] S. Luo, J. Bimbo, R. Dahiya, and H. Liu, "Robotic tactile perception of object properties: A review," *Mechatronics*, vol. 48, pp. 54–67, 2017.

[15] R. S. Dahiya, G. Metta, M. Valle, and G. Sandini, "Tactile sensing—From humans to humanoids," *IEEE Transactions on Robotics*, vol. 26, no. 1, pp. 1–20, 2010.

[16] O. Azulay et al., "AllSight: A low-cost and high-resolution round tactile sensor with zero-shot learning capability," *IEEE Robotics and Automation Letters*, vol. 9, no. 1, pp. 483–490, 2024.

[17] M. H. Tippur and E. H. Adelson, "GelSight360: An omnidirectional camera-Based tactile sensor for dexterous robotic manipulation," in *2023 IEEE International Conference on Soft Robotics (RoboSoft)*, 2023, pp. 1–8.

[18] C. Lin, H. Zhang, J. Xu, L. Wu, and H. Xu, "9DTact: A compact vision-based tactile sensor for accurate 3D shape reconstruction and generalizable 6D force estimation," *IEEE Robotics and Automation Letters*, vol. 9, no. 2, pp. 923–930, 2024.

[19] H. Li et al., "BioTacTip: A soft biomimetic optical tactile sensor for efficient 3D contact localization and 3D force estimation," *IEEE Robotics and Automation Letters*, vol. 9, no. 6, pp. 5314–5321, 2024.

[20] W. Fan, H. Li, W. Si, S. Luo, N. Lepora, and D. Zhang, "ViTacTip: Design and verification of a novel biomimetic physical vision-tactile fusion sensor," in *2024 IEEE International Conference on Robotics and Automation (ICRA)*, 2024, pp. 1056–1062.

[21] G. Vitrani, B. Pasquale, and M. Wiertlewski, "ShadowTac: Dense measurement of shear and normal deformation of a tactile membrane from colored shadows," in *2025 IEEE International Conference on Robotics and Automation (ICRA)*, 2025, pp. 5004–5010.

[22] M. Li et al., "EasyCalib: Simple and low-cost in-situ calibration for force reconstruction with vision-based tactile sensors," *IEEE Robotics and Automation Letters*, vol. 9, no. 9, pp. 7803–7810, 2024.

[23] A.-H. Shahidzadeh, G. M. Caddeo, K. Alapati, L. Natale, C. Fermüller, and Y. Aloimonos, "FeelAnyForce: Estimating contact force feedback from tactile sensation for vision-based tactile sensors," in *2025 IEEE International Conference on Robotics and Automation (ICRA)*, 2025, pp. 251–257.

[24] Z. Motyka, "Fractal moiré interferometry," *Chaos Solitons Fractals*, vol. 153, no. 111396, p. 111396, Dec. 2021.

[25] J. Ning, L. Xie, Z. Yan, Y. Bu, and J. Luo, "MoiréVision: A generalized Moiré-based mechanism for 6-DoF motion sensing," in *Proceedings of the 30th Annual International Conference on Mobile Computing and Networking*, Washington D.C., DC, USA, 2024, pp. 467–481.

[26] J. Zuo and T. Takaki, "Force visualization system integrating moiré fringe with fiber optic plates to eliminate parallax error," *ROBOMECH Journal*, vol. 12, no. 1, p. 17, 2025.

[27] L. Luo et al., "Compdvision: Combining near-field 3D visual and tactile sensing using a compact compound-eye imaging system," in *2024 IEEE/RSJ International Conference on Intelligent Robots and Systems (IROS)*, 2024, pp. 262–268.

[28] E. Roberge, G. Fornes, and J.-P. Roberge, "StereoTac: A novel visuotactile sensor that combines tactile sensing with 3D vision," *IEEE Robotics and Automation Letters*, vol. 8, no. 10, pp. 6291–6298, 2023.

[29] S. Zhang et al., "TIRgel: A visuo-tactile sensor with total internal reflection mechanism for external observation and contact detection," *IEEE R obotics and Automation Letters*, vol. 8, no. 10, pp. 6307–6314, 2023.

[30] S. Li et al., "JamTac: A tactile jamming gripper for searching and grasping in low-visibility environments," *Soft Robotics*, vol. 10, no. 5, pp. 988–1000, 2023.

[31] A. SaLoutos, E. Stanger-Jones, M. Guo, H. Kim, and S. Kim, "Design of a multimodal fingertip sensor for dynamic manipulation," in *2023 IEEE International Conference on Robotics and Automation (ICRA)*, London, United Kingdom: IEEE, May 2023, pp. 8017–8024.

[32] S. Li et al., "M3Tac: A multispectral multimodal visuotactile sensor with beyond-human sensory capabilities," *IEEE Transactions on Robotics*, vol. 40, pp. 4484–4503, 2024.